Linear Evolution of Error Covariances in a Quasigeostrophic Model

Chris Snyder

National Center for Atmospheric Research,* Boulder, Colorado

Thomas M. Hamill

NOAA–CIRES Climate Diagnostics Center, Boulder, Colorado

Stanley B. Trier

National Center for Atmospheric Research, Boulder, Colorado

ABSTRACT

The characteristics of forecast-error covariances, which are of central interest in both data assimilation and ensemble forecasting, are poorly known. This paper considers the linear dynamics of these covariances and examines their evolution from (nearly) homogeneous and isotropic initial conditions in a turbulent quasigeostrophic flow qualitatively similar to that of the midlatitude troposphere. The experiments use ensembles of 100 solutions to estimate the error covariances. The error covariances evolve on a timescale of $O(1$ day), comparable to the advective timescale of the reference flow. This timescale also defines an initial period over which the errors develop characteristic features that are insensitive to the chosen initial statistics. These include 1) scales comparable to those of the reference flow, 2) potential vorticity (PV) concentrated where the gradient of the reference-flow PV is large, particularly at the surface and tropopause, and 3) little structure in the interior of the troposphere. In the error covariances, these characteristics are manifest as a strong spatial correlation between the PV variance and the magnitude of the reference-flow PV gradient and as a pronounced enhancement of the error correlations along reference-flow PV contours. The dynamical processes that result in such structure are also explored; the key is the advection of reference-flow PV by the error velocity, rather than the passive advection of the errors by the reference flow.

1. Introduction

Estimates of forecast-error covariances are crucial for statistical data assimilation schemes, yet little is known about the form of error covariances or their relation to the flow in the atmosphere or ocean at a given instant. Most existing information comes from fitting stationary, isotropic covariance models to differences between observations and short-range forecasts (e.g., Hollingsworth and Lönnberg 1986), and similar models are in turn assumed in all present operational assimilation schemes. The extent to which such stationary, isotropic covariances approximate the true forecast-error covariances is still an open question.

The form and magnitude of forecast-error covariances reflect both the prior evolution of errors during the forecast and the modification of those errors by the assimilation of new observations. The present paper focuses on the former process and considers the evolution of error covariances beginning from an isotropic initial error distribution. For simplicity, we employ a high-resolution quasigeostrophic channel model and examine the covariance evolution in the limit of small errors; that is, the error evolution is assumed to be governed by dynamics linearized about a reference solution, which consists of a turbulent jet with superimposed baroclinic waves. Our specific interests include the timescales for covariance evolution, the typical structure (particularly the anisotropy) of forecast-error covariances, and the relation of that structure to the reference flow. A companion paper (Hamill et al. 2002) examines the structure and flow dependence of analysis errors in a cycling forecast-analysis system, and addresses the extent to which covariance structure produced by the dynamics (and described here) survives the assimilation of observations.

For all but the simplest systems, explicit evolution of error covariances is a formidable calculation. Contin-

uous systems require the solution of a partial differential equation in twice the number of spatial dimensions of the original system (Cohn 1993 and references therein). For discrete systems, such as our quasigeostrophic model, the problem becomes the evolution of a covariance matrix whose size scales as the square of the number of degrees of freedom of the system.

Here, we employ an approximate, Monte Carlo technique, first sampling the errors (or, as we will frequently refer to them, perturbations) from a specified initial distribution, then evolving the ensemble forward in time and examining the properties of the sample covariance matrix. In most of our simulations, the ensemble size is $O(100)$ while the model possesses nearly 10^5 degrees of freedom. By contrast, it is often assumed in ensemble forecasting (Molteni et al. 1996; Toth and Kalnay 1997) that directly sampling from the initial error distribution is of limited utility with such small ensembles, as the inherent sampling error may overwhelm the desired covariance information. An important question, which we will also address briefly, is the extent to which small ensembles directly sampled from the initial error distribution can provide useful covariance estimates.

Because of the difficulty of evolving error covariances, there is scant literature pertaining to the development of anisotropy and its relation to the reference flow. Cohn (1993) presents an analytic theory for error-covariance evolution in univariate partial differential equations; while including examples of interest (such as the advection of a passive scalar), this theory does not encompass more complicated systems such as two-dimensional barotropic flow. That system was studied in its continuous form by Thompson (1986), who showed analytically that, given homogeneous, isotropic initial errors, the initial growth of error enstrophy (vorticity variance) arose from the development of anisotropy in the errors and was concentrated in regions where the vorticity gradient of the reference flow was large. In experiments with an extended Kalman filter, Evensen (1992) explicity evolved error covariances for a low-resolution quasigeostrophic model and showed that evolving the covariances based only on advection by the reference flow (and thus ignoring the interaction of the errors with the reference-state potential vorticity gradients) was a poor approximation to the full evolution. Bouttier (1993) also explicitly evolved error covariances but in a low-resolution, spherical barotropic model and found anisotropic signatures of Rossby wave propagation and advection by the reference flow within one day. The baroclinic, primitive equation problem was considered by Todling and Ghil (1994), but only in the context of a two-layer model and using a broad zonal jet as the reference flow. Finally, Fischer et al. (1998) evolved error covariances for a semigeostrophic model with uniform interior potential vorticity. Like Thompson (1986), they note a tendency for the error variance to be concentrated where the gradients of potential vorticity are large in the reference flow.

Dynamical systems theory provides further guidance concerning covariance evolution, at least in the limit of long times and small errors. If we make an infinitesimally small perturbation to the initial state of a nonlinear system, that perturbation will converge after sufficient time to a specific direction, known as the first Lyapunov vector. This direction depends on the state of the system (and thus varies in time) but is independent of the initial perturbation. More generally, a set of n infinitesimal perturbations will converge to the subspace spanned by the first n Lyapunov vectors. [See Legras and Vautard (1995) for further discussion and references, and Snyder and Hamill (2003, hereafter SH) for the properties of the leading Lyapunov vectors of the quasigeostrophic flow considered here.] Ignoring nonlinear effects, error covariances must then, in the limit $t \rightarrow \infty$, reflect the structure of the leading Lyapunov vectors. In section 5, we will investigate whether the convergence to the leading Lyapunov vectors is significant over finite time intervals of a day or two.

As already mentioned, our primary motivation for exploring covariance evolution is to characterize the flow dependence and anisotropy of short-range forecast-error covariances required in statistical data assimilation. While it is clear that dynamics influence the error covariances over the course of the short-range forecast itself, the influence of the dynamics also extends beyond the previous analysis into the recent past, as the errors in that analysis arose from both observation errors and errors in the previous short-range forecast, and those forecast errors were in turn influenced by even earlier analyses and forecasts. Thus, in what follows we will consider the covariance evolution over forecasts of a few days, rather than restricting our attention to the 6- or 12-h forecasts typically used in global or synoptic-scale assimilation schemes. This view of the problem as series of short-range forecasts followed by analyses also provides some justification for considering only linear dynamics, as existing evidence (Errico et al. 1993; Gilmour et al. 2001) indicates forecast errors at synoptic scales evolve linearly over the first 12–48 h of the forecast. To see the relevance of our calculations to errors in a cycling forecast-analysis system, we refer the reader to the companion paper (Hamill et al. 2002).

Lacking a useful theory for error-covariance evolution in our system, we adopt an experimental approach. Section 2 provides details of the numerical experiments; the covariance evolution is estimated, as mentioned previously, by drawing a random sample of initial perturbations from a specified Gaussian distribution and then evolving that sample forward in time using dynamics linearized about the reference solution. A description of the quasigeostrophic model also appears in section 2. Following the description of the numerical experiments, section 3 documents the qualitative resemblance of the reference solution to midlatitude synoptic-scale flows. Of particular importance for the perturbation evolution is the fact that by far the largest potential-vorticity gra-

dients are found, as in the atmosphere, at the surface and the lid (the model's version of the tropopause). Section 4 then presents results for the error-covariance evolution, which show that within 1–2 days the covariances have become highly anisotropic and possess a well-defined relation to the reference flow. On this same time-scale of 1–2 days, there is also substantial convergence of the perturbations into the subspace of the first 20 Lyapunov vectors (section 5). We discuss various aspects of the perturbation dynamics in section 6, including the role of reference-state potential-vorticity gradients and of dissipation. The paper concludes with a summary and a discussion of some implications of our results.

2. The numerical experiments

a. The quasigeostrophic model

We consider Boussinesq quasigeostrophic flow having constant buoyancy frequency N and confined to a zonally periodic channel bounded meridionally and at top and bottom by rigid surfaces. The flow is driven by Newtonian relaxation to a specified baroclinic zonal jet. An Ekman layer at the surface and a weak numerical smoothing provide dissipation.

Most of the subsequent discussion will use nondimensional variables obtained by scaling vertical distance by H, the depth of the channel; horizontal distance by the Rossby radius NH/f, where f is the Coriolis parameter; velocities by U, the maximum speed of the jet toward which the flow is relaxed; and time by the advective timescale, fU/NH.

In the nondimensional variables, the flow is governed by the evolution equations for the pseudo–potential vorticity q (PV hereafter),

$$\frac{\partial q}{\partial t} + \mathbf{v} \cdot \nabla q = (-\tau^{-1} + D)(q - q^e), \qquad (1a)$$

and for the potential temperature θ (a deviation from the constant background stratification) at the surface and lid,

$$\frac{\partial \theta}{\partial t} + \mathbf{v} \cdot \nabla \theta = \begin{cases} -\Gamma\left(\dfrac{\partial^2}{\partial x^2} + \dfrac{\partial^2}{\partial y^2}\right)\phi \; + (-\tau^{-1} + D)(\theta - \theta^e), & \text{at } z = 0 \\ (-\tau^{-1} + D)(\theta - \theta^e), & \text{at } z = 1. \end{cases} \qquad (1b)$$

Here, the streamfunction ϕ is related to velocity and temperature by $(u, v, \theta) = (-\partial\phi/\partial y, \partial\phi/\partial x, \partial\phi/\partial z)$, and to q and θ through

$$q = \beta y + \partial^2\phi/\partial z^2 + \nabla^2\phi, \qquad (2)$$

with boundary conditions $\partial\phi/\partial z = \theta$ at $z = 0, 1$. In addition, $\mathbf{v} = (u, v)$ is the horizontal velocity, ∇ is the horizontal gradient operator, τ is the relaxation time, and the superscript e indicates the zonal state toward which the flow is relaxed. We choose $q^e = \beta y$ and u^e given by (17) in Hoskins and West (1979) with their parameter $\mu = 1$; ϕ^e and θ^e may be inferred from u^e and the geostrophic and hydrostatic relations. The parameter $\Gamma = (A_v/2f)^{1/2}N/U$, where A_v is the coefficient of vertical eddy viscosity, controls the Ekman pumping (Pedlosky 1987, his section 4), and D is a numerical smoothing operator defined by

$$D = -\nu(\partial^4/\partial x^4 + \partial^4/\partial y^4).$$

This smoothing controls the buildup of potential enstrophy at the smallest resolved scales.

The flow has periodicity x_L in x. On the channel walls at $y = 0, y_L$, both the normal flow and zonal-mean acceleration are zero (Pedlosky 1987); thus,

$$\phi' = \partial^2\overline{\phi}/\partial y\partial t = 0 \quad \text{on } y = 0, y_L, \qquad (3)$$

where an overbar indicates a zonal (x) average and a prime the deviation from that average. If we assume that $\partial\overline{\phi}/\partial y = -u^e$ at the initial time, then the latter condition in (3) may be replaced by

$$\partial(\overline{\phi} - \phi^e)/\partial y = 0 \quad \text{on } y = 0, y_L, \qquad (4)$$

The dissipative terms in (1) require additional wall conditions for higher y derivatives. As discussed below, the Poisson problem for ϕ given q is solved numerically using a spectral expansion; wall conditions consistent with the assumed expansion and with (3) and (4) are

$$\partial^{2n}\phi'/\partial y^{2n} = \partial^{2n+1}(\overline{\phi} - \phi^e)/\partial y^{2n+1} = 0$$
$$\text{on } y = 0, y_L, \qquad (5)$$

for $n = 0, \ldots, 3$.

The numerical solution of (1)–(4) uses standard techniques. The variables q and ϕ are defined on a discrete grid with N vertical levels at heights $z_{\hat{n}} = (\hat{n} - 1/2)/N$, while θ is defined at $z = 0, 1$. Advective terms are represented as in Arakawa (1966) and are integrated in time using a leapfrog scheme; the dissipative terms use a forward Euler time step and are lagged for stability. The Poisson equation (2) for ϕ is discretized with second-order, centered differences and solved by a direct method assuming a solution of the form

TABLE 1. Values of nondimensional and dimensional parameters. Where a nondimensional parameter has an obvious dimensional counterpart, it is also given.

Parameter	Nondimensional value	Dimensional value
U		60 ms^{-1}
N		1.1×10^{-2} s^{-1}
f		10^{-4} s^{-1}
β	0.27	1.6×10^{-11} m^{-1} s^{-1}
H		9.0 km
y_L	8.0	8.1×10^3 km
x_L	16.0	16.0×10^3 km
τ	0.98×10^{-2}	20 d
A_v		5 m^2 s^{-1}
Γ	0.30	
ν	1.9×10^{-5}	

$$g(x_{\hat{k}}, y_{\hat{m}}, z_{\hat{n}}) = \sum_{m=1}^{M} a_{0m\hat{n}} \cos(m\hat{m}\pi/M)$$

$$+ \sum_{k=1}^{K-1} \sum_{m=1}^{M-1} a_{km\hat{n}} \exp(ik\hat{k}2\pi/K)$$

$$\times \sin(m\hat{m}\pi/M), \qquad (6)$$

where g is any of q, ϕ, or θ; $(x_{\hat{k}}, y_{\hat{m}}, z_{\hat{n}})$ gives the gridpoint locations; and K and M are the number of grid points in x and y, respectively. Further details may be found in the appendix of Rotunno and Bao (1996).

The simulations presented below use $K = 128$, $M = 64$, $N = 8$, and the parameter values specified in Table 1. The velocity scale U, which sets the timescale for the simulations, was chosen to give an average error-doubling time of approximately 2 days (SH). The relaxation time τ and the smoothing coefficient ν were chosen to be as small as possible while still maintaining a turbulent and well-resolved reference solution. Other parameters have values typical of the midlatitude troposphere.

In employing this quasigeostrophic (QG) model, our goal is not to reproduce the atmospheric general circulation. Rather, we seek a system that is intermediate in complexity (and computational burden) between low-order systems and numerical weather prediction models, and that retains qualitative characteristics of synoptic-scale atmospheric flows.

As our goal is not realism, we have made several simplifications to the physics contained in (1)–(5). First, the relaxation is applied to the PV, rather than to the temperature as in some simple models of radiative relaxation. Second, the wall boundary conditions (5) do not correspond to an obvious physical system. In addition, those wall conditions are not consistent with the surface Ekman layer, in that the Ekman layer implies a mass flux at the walls that should be taken up by wall layers but is ignored here. We have chosen (5) for computational simplicity since the channel walls themselves are unrealistic.

In the figures that follow, we will employ for con-

venience the generalized PV $\tilde{q}$ rather than q. The generalized PV is identical to q at each vertical level except the first and last ($j = 1$, N), where it is defined by

$$\tilde{q}_1 = q_1 + N \times \theta_0, \qquad \tilde{q}_N = q_N - N \times \theta_N, \quad (7)$$

with θ_0 and θ_N the potential temperature at the surface and lid, respectively. Equation (7) is the discretized version of Bretherton's (1966) identification of the boundary θ as a δ function of PV. Where there is no danger of confusion below, we will simply refer to $\tilde{q}$ as the PV and omit tildes.

b. The tangent linear model

Suppose we are given a solution $\overline{\phi}(x, y, z, t)$ of (1), which we will refer to subsequently as the reference solution or the reference state. The evolution of sufficiently small perturbations to the reference state is approximated by the linearized equation,

$$\partial q'/\partial t + \overline{\mathbf{v}} \cdot \nabla q' + \mathbf{v}' \cdot \nabla \overline{q} = (-\tau^{-1} + D)q', \quad (8)$$

along with similar equations [derived from (1b)] for θ'. Bars in (8) denote quantities associated with the reference state, while primes denote perturbations. All boundary conditions for (1) are linear and thus are unchanged for the linearized equations.

The linearized equations are solved using the same discretization as for the nonlinear equations. In practice, this means that the discretized form of (8), for example, is obtained by linearizing the discretized form of (1a).

c. Ensembles of initial perturbations

As discussed in the introduction, ensembles of initial perturbations will be drawn randomly from a specified probability distribution. Such a sample would ideally be drawn from the distribution of analysis error, which would depend on the location and accuracy of recent observations, the state of the flow, and on the data-assimilation scheme. Even in a simple model such as this, however, the analysis-error distribution is difficult to compute and is poorly known. The properties of that distribution are considered further in Hamill et al. (2002).

Here, we simply sample the initial perturbations from specified, multivariate normal distributions. Since the correct initial distribution is uncertain, three different distributions, and thus three different initial ensembles, will be considered in order to assess how the results depend on the choice of distribution. The three distributions are related to three common inner products: energy, potential enstrophy, and squared streamfunction. We will refer to the corresponding initial ensembles as the energy ensemble, the potential-enstrophy ensemble, and the streamfunction ensemble.

The distributions and initial ensembles are derived from the inner products as follows. Let $\mathbf{x}$ be a vector whose components are the spectral coefficients from an

expansion of ϕ' as in (6). [One could equally well consider perturbations in the gridpoint space, as long as they are restricted to the subspace defined by the boundary conditions (3) and (4).] Next, let $\mathbf{S}$ be a matrix that specifies one of the inner products; that is, $\mathbf{x}^T \mathbf{Sx}$ gives the norm of the perturbation in the specified inner product. For each inner product, an initial ensemble is then obtained by taking $\mathbf{C} = \mathbf{S}^{-1}$ and sampling $\mathbf{x}$ from $N(\mathbf{0}, \mathbf{C})$, the multivariate normal distribution with mean $\mathbf{0}$ and covariance $\mathbf{C}$. Definitions of the inner products and details of the sampling procedure are given in the appendix.

These choices for $\mathbf{C}$ have the practical appeal that constructing random samples from $N(\mathbf{0}, \mathbf{C})$ is straightforward. Although it has been suggested (e.g., Palmer et al. 1998) that the energy ensemble provides a rough approximation, we emphasize that none of these choices for $\mathbf{C}$ can fully capture the characteristics of analysis errors. In particular, they do not reflect the dependence of analysis errors on the observing network or the dynamics of the flow, which Hamill et al. (2002) show is substantial.

Still, the relation of $\mathbf{C}$ to physical inner products provides two useful properties. First, the probability of a perturbation depends only on its length in the chosen norm, since $N(\mathbf{0}, \mathbf{C})$ has probability density that is proportional to $\exp(-\mathbf{x}^T \mathbf{C}^{-1} \mathbf{x})$. Thus, for example, two perturbations of equal energy are equally likely to appear in the energy ensemble, and perturbations with smaller energy are more likely than those with large energy. This property also illustrates how the typical member varies among the different ensembles. In broad terms, perturbations in the potential-enstrophy ensemble on average have larger spatial scales than those in the energy ensemble, since of two perturbations with equal energy, the one with smaller scale will have larger potential enstrophy. Perturbations from the streamfunction ensemble, on the other hand, will have smaller spatial scales on average than those in the energy ensemble.

Second, if the perturbations are projected onto singular vectors computed for the norm defined by $\mathbf{S}$, the projection coefficients are independent and have equal variance, so that the perturbations project equivalently onto each singular vector. To see this, let $\mathbf{U}$ be the matrix whose columns are the initial SVs for the norm defined by $\mathbf{S}$. Since the SVs are orthogonal with respect to this inner product, $\mathbf{U}^T \mathbf{SU} = \mathbf{I}$. Let $\mathbf{x}$ be a random vector with distribution $N(\mathbf{0}, \mathbf{S}^{-1})$, so that $\langle \mathbf{xx}^T \rangle = \mathbf{S}^{-1}$ where $\langle \cdot \rangle$ denotes the expected value. Now project $\mathbf{x}$ onto the initial singular vectors; that is, write $\mathbf{x} = \mathbf{Ua}$ for a vector $\mathbf{a}$ of projection coefficients. Then $\mathbf{U} \langle \mathbf{aa}^T \rangle \mathbf{U}^T = \mathbf{S}^{-1}$ and multiplication by $\mathbf{U}^T \mathbf{S}$ on the right and by $\mathbf{SU}$ on the left gives $\langle \mathbf{aa}^T \rangle = \mathbf{I}$.

3. The reference solution

Although our primary interest in what follows will be the behavior of small perturbations to this state, we

a) *PV, streamfunction at top, t = 120 d*
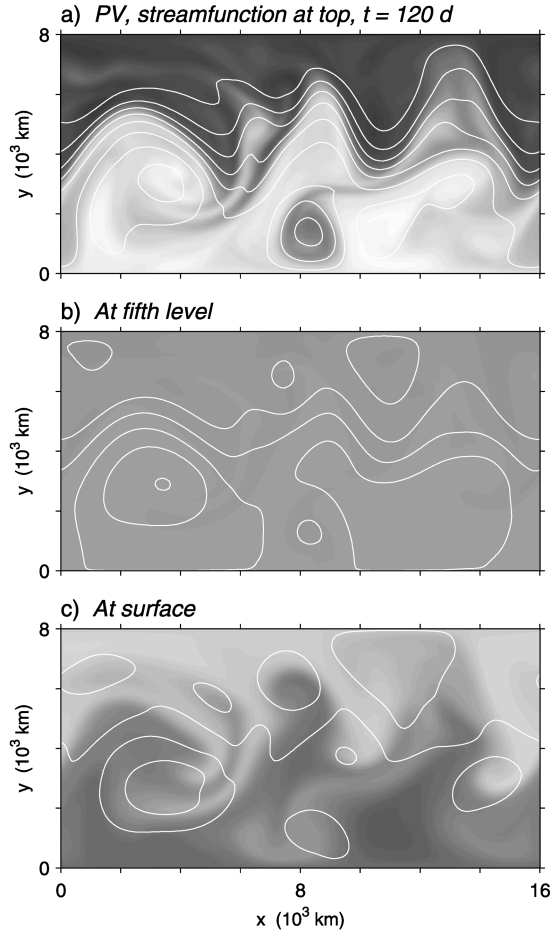
b) *At fifth level*

c) *At surface*

FIG. 1. Reference-state fields at $t = 120$ days at (a) the uppermost model level, (b) model level 5, and (c) the lowest model level. Nondimensional generalized PV is shaded with the darkest gray (white) corresponding to a value of 16 (-16); white lines are contours of the nondimensional streamfunction (interval 0.4).

pause here to document general characteristics of the reference solution. The reference integration uses the parameters given above and begins at $t = -240$ days with a localized disturbance in $\bar{q}$ at $z = 1$ superposed on the "relaxed" zonal state (specified by q^e). Following the spinup of a statistically steady, turbulent state, the reference solution is taken to be the solution for $0 < t < 200$ days.

The flow at any instant, an example of which is shown in Fig. 1, is qualitatively similar to that of the midlatitude troposphere. It is characterized by a meandering, baroclinic westerly jet, whose speed increases from the surface to the model lid. The large-amplitude waves, which typically have zonal wavenumber between 2 and 4 (in units of cycles per domain length, or dimensional wavelength between 4000 and 8000 km), propagate along the jet from west to east and frequently break to form cutoff vortices. Examination of Hovmöller diagrams for meridional velocity at the lid (not shown) reveals that the waves are also frequently organized into

packets, much as occurs in the atmosphere and in other simplified primitive equation and quasigeostrophic simulations (Lee and Held 1993). Since the forcing and dissipation operators are zonally symmetric, all zonal asymmetries are produced internally by the dynamics.

The structure of the (generalized) potential vorticity $\overline{q}$ is of particular interest. In $\overline{q}$ at top and bottom (Figs. 1a,c), strong horizontal gradients are concentrated in a narrow zone that follows the meandering jet; this is particularly evident at the lid, where the gradients are largest and most coherent. At midheight ($z = 0.5$; Fig. 1b), there is little systematic organization in the horizontal gradient of $\overline{q}$, and the general appearance is of a tracer being mixed in the center of the channel.

The observed troposphere has similar structure in PV. At the surface, horizontal gradients in θ (and thus of generalized PV) are largest in a zone that follows the jet, while PV gradients are weak and have little organization in the interior of the troposphere, at least away from regions of strong ascent and latent heating. By far the strongest gradients are to be found at the sloping tropopause in a narrow zone that again follows the jet (Hoskins et al. 1985), much as in Fig. 1 if we interpret the model's lid to represent the tropopause.

The relative strength of $\overline{q}$ gradients at the surface and lid in the reference solution means that PV anomalies on the boundaries (with respect to, say, a zonal average) are typically larger than interior PV anomalies. In fact, the flow associated with the boundary PV anomalies, obtained by inverting (2), has rms velocities that are more than twice that associated with the interior $\overline{q}$ anomalies. Inversion of observed PV anomalies yields similar results (Davis 1992).

The time-mean energy cycle is also qualitatively similar to that of the atmosphere (Peixoto and Oort 1992, their Fig. 14.8), and illustrates the nature and maintenance of the reference solution. As in the atmosphere, deviations from the zonal mean (eddies) draw potential energy from the zonal-mean flow via baroclinic conversion, while the eddies transfer kinetic energy to the mean flow through barotropic conversion. The mean flow is driven by the relaxation, which generates both mean kinetic and potential energy at the same time it damps the eddies. Consistent with this driving, the time- and zonal-mean jet has maximum speed that is 7/10 of the maximum u^e (or about 40 m s^{-1}). Ekman pumping is also a significant sink of both mean and eddy kinetic energy, while the explicit smoothing has a negligible direct influence on the energy cycle.

The kinetic energy spectrum (Fig. 2) is another traditional diagnostic for turbulent flows. Since the flow is statistically homogeneous only in x, we compute the one-dimensional spectrum for zonal Fourier components, evaluated at midchannel and on the lid ($y = y_L/2, z = 1$). As was evident from Fig. 1, the energy-containing range encompasses the longest waves in the channel, with a peak at wavenumber 3. There is also a well-defined inertial range, in which kinetic energy obeys a power-
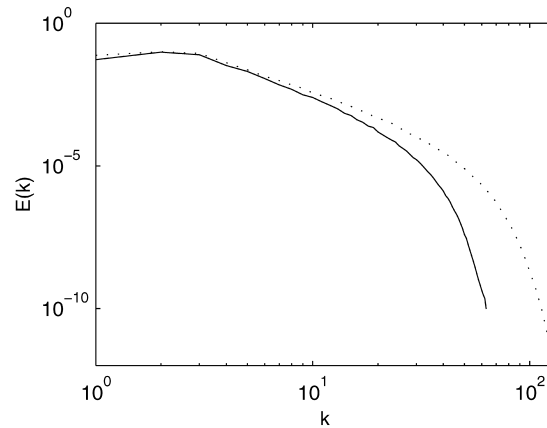

FIG. 2. Time-averaged power spectra of kinetic energy for the reference solution at $y = y_L/2$, $z = 1$. The dotted line shows the spectrum from a run with doubled resolution and ν reduced by a factor of 8.

law decay with a spectral slope somewhat shallower than -3. Atmospheric observations exhibit spectra with inertial ranges having similar power laws (Boer and Shepherd 1983); any quantitative agreement with these quasigeostrophic results, however, is probably fortuitous.

We have also briefly examined the sensitivity of the reference solution to model parameters and resolution. Doubling the resolution and reducing the smoothing coefficient ν by a factor of 8 has little effect on the energy-containing scales, as might be expected from the negligible role of the numerical smoothing in the energy budget, but has a profound effect at the smallest scales, as would be predicted by the theory of two-dimensional turbulence. Both results are evident in Fig. 2, where the kinetic energy spectrum at doubled resolution is indicated by a dotted line. In the physical coordinates, gradients in PV and boundary θ increase substantially at doubled resolution while the larger-scale character of the solution is unchanged.

There is little sensitivity to varying other parameters except β. Doubling or halving either the strength of the Ekman pumping or the relaxation timescale, produces little qualitative change in the solution. A doubling of β, however, leads to solutions in which wave packets are more frequent and coherent; a further doubling produces an almost periodic solution consisting of a single wave packet recirculating through the channel (see Lee and Held 1993).

4. Covariance evolution

As discussed in section 2c, the ensemble of perturbations is initialized as a random sample from a specified Gaussian distribution. Evolution under the linearized dynamics then modifies the ensemble and its statistics. This section examines how the ensemble statistics change from their initial conditions, the relation of
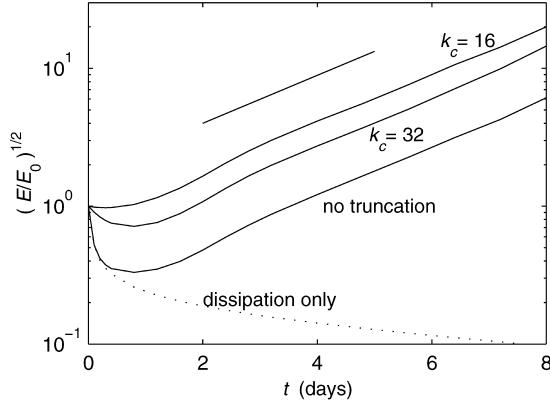
FIG. 3. The square root of total perturbation energy, normalized by its value at $\Delta t = 0$, as a function of Δt. The short, sloping line segment shows growth at the rate of the leading Lyapunov exponent.
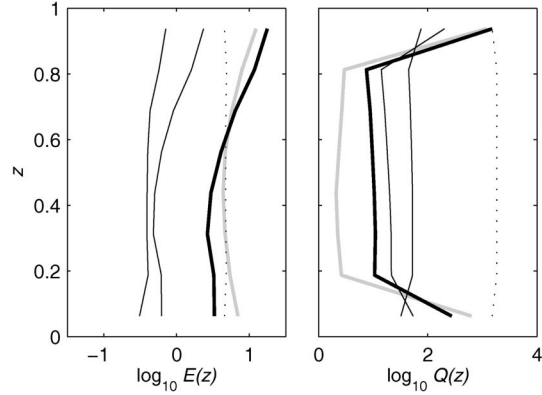

FIG. 4. Area-averaged perturbation total energy $E(z)$ and potential enstrophy $Q(z)$ at $\Delta t = 0$ (dotted lines), 20 h (solid), 2 days (solid), and 4 days (thick solid). After $\Delta t = 0$, E increases at each Δt shown, while Q in the interior of the troposphere decreases monotonically at each Δt shown. Thick gray lines indicate the time-averages of $E(z)$ and $Q(z)$ for deviations of the reference state from its time mean; each has been scaled for display so that its vertical integral is the same as that of the corresponding perturbation quantities at $\Delta t = 4$d. Perturbation results are averaged over an ensemble of 10 perturbations and over 10 initial times.

those changes to the reference flow, and the timescale over which they occur. Most of the results are not sensitive to the initial ensemble statistics, so we will concentrate on the energy ensemble, except in section 4d where a number of other ensembles are discussed.

a. Averaged characteristics

Results in this subsection (and "averaged" results elsewhere) are computed as averages over both ensembles of initial perturbations and over 11 initial times from $t = 0$ to $t = 100$ days at intervals of 10 days. Except where noted, each ensemble has 100 members.

The behavior of the perturbation energy as a function of time is shown in Fig. 3, averaged over the ensemble and over initial times. For the first day, the energy decays. This initial decay is follow by amplification that becomes exponential for $t > 3$ days, with a rate that closely approximates the leading Lyapunov exponent of 0.8 day^{-1} (SH). Note that steady exponential growth is not seen in integrations from a single initial time, but rather arises from averaging over initial times.

The initial decay is tied to the dissipation in the model. If the adiabatic dynamics are ignored in (8) and the perturbations allowed to evolve under the influence of the Ekman pumping, relaxation, and numerical smoothing alone, then the initial decay is barely altered, as indicated by the dotted curve in Fig. 3. In addition, the decay diminishes or disappears if the smallest horizontal scales are truncated from the initial perturbations, that is, if waves with $(k^2 + m^2)^{1/2} > k_c$ have their amplitudes set to zero. The cases $k_c = 16, 32$ are shown in Fig. 3. Wirth and Ghil (2000) document similar initial decay of perturbations in a primitive equation ocean model and discuss the relation of the decay to the model's dissipation. A more complete discussion of the role of the dissipation is deferred to section 6.

It is clear from Fig. 3 that by $t = 1$ day the dissipation

no longer controls the perturbation evolution, as all the experiments that include the adiabatic dynamics behave similarly by this time. There follows a transient period of growth out to $t \approx 3$ days, after which the long-term exponential growth begins. This timescale of 1–3 days for the transient adjustment of the ensemble properties under the influence of the dynamics will be seen repeatedly in what follows.

The timescale that would be inferred from Fig. 3 is largely independent of the norm chosen to quantify the perturbation amplitude. Measuring the perturbations in either the squared streamfunction or potential enstrophy merely alters the details of the transient period (not shown). For example, squared streamfunction, which gives little weight to the small scales that are strongly dissipated, exhibits little decay, while the decay of potential enstrophy is greater than that in Fig. 3. Regardless of the norm, however, the averaged growth becomes nearly exponential after $t = 3$ days.

The variation of the perturbation amplitude with height, and its evolution in time, are illustrated by Fig. 4, which shows the area-integrated energy and potential enstrophy at $t = 0$, 20 h, 2 and 4 days after the initialization of the ensembles. Results are again averaged over ensembles and over initial times.

The energy at initial times is uniform with height to within sampling error, while the enstrophy has weak minima at the first and last grid levels. Consistent with Fig. 3, both quantities decay substantially over the first day and then begin to increase. As the perturbations evolve, the energy develops a peak at the model lid and a minimum in the mid- to lower troposphere. The development of the potential enstrophy is more dramatic; initial decay is accompanied by growth at both upper-
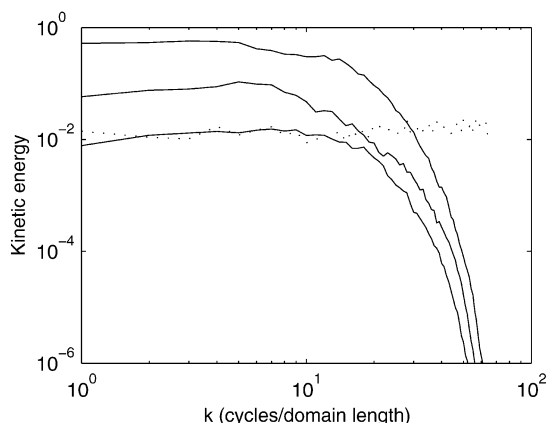
FIG. 5. Spectra of perturbation kinetic energy at $y = y_L/2$, $z = 1$ at various times. Shown are $\Delta t = 0$ (dotted line), 20 h, 1 day, 2 days (solid lines; larger kinetic energy corresponds to larger Δt). Results are averaged over an ensemble of 10 perturbations and over 10 initial times.

and lowermost levels, with the enstrophy at the uppermost level exceeding that in the interior by two orders of magnitude after 4 days. The energy and enstrophy profiles by 4 days are both similar to those for the leading Lyapunov vector (SH, see their Fig. 2) and for analysis errors in this system (Hamill et al. 2002, their Figs. 6, 7). Beyond 4 days, the profiles' shape changes little although their growth continues (not shown).

Thus, on average the perturbations evolve from having PV distributed throughout the troposphere to having PV concentrated at the upper and lower boundaries. The distribution of energy with height reflects a smoothed version of this process, consistent with (2). As noted in section 3, the reference solution has similar properties, with relatively weak PV in the interior and winds maximized near either boundary; this is shown in Fig. 4 by the thick gray curves, which represent the profiles for deviations in the reference state from the time and zonal mean.

Finally, consider the evolution of the horizontal scale of the perturbations. Figure 5 displays the power spectrum of kinetic energy at the center of the channel as a function of zonal wavenumber. Initial decay is strongest at small scales, consistent with dissipation (particularly the numerical smoothing) causing the decay. Growth begins first at wavenumbers less than 10, which contain the most energy in the reference-state flow. By $t = 2$ days, the shape of the spectrum becomes fixed and growth occurs systematically at all scales, again indicating a timescale of 1–3 days for the perturbations to approach their asymptotic properties. The asymptotic spectrum decays with wavenumber more slowly than the reference-state spectrum (Fig. 2), much like the spectrum of the leading Lyapunov vector (SH, their Fig. 3).

b. Adjustment to $\nabla \overline{q}$

To this point, we have seen that the growth of perturbations becomes on average, exponential following a transient period of 1–3 days, and that this same transient period is associated with changes from the initial spatial structure (implied by the chosen covariance matrix **C**) to dynamically determined structure whose characteristics are largely independent of the initial conditions. In particular, perturbations evolve to have PV concentrated at the top and bottom boundaries (with little PV in the interior of the flow), the perturbation velocities become concentrated at top and bottom as well, and perturbations develop a characteristic horizontal spectrum that decays with wavenumber but is less steep than the reference-state spectrum.

The growth of PV perturbations at top and bottom shown in Fig. 4 is striking, particularly when compared to the steady decay in the interior over the same time interval. To gain more insight into this behavior and into the perturbation dynamics in general, we examine next the evolution of the perturbation variance for a specific initial time, $t = 120$ days.

Figure 6 displays the PV variance at the uppermost level for an ensemble with initial perturbations drawn from the distribution implied by the energy norm. The variance is shown at $\Delta t = 5$, 10, and 20 h. The initial variance (not shown) is nearly uniform over the domain except for sampling error.

Two points are noteworthy. The first is the rapid emergence of structure in the PV variance as the perturbations evolve. This structure emerges through growth of the variance in a narrow, meandering band in the central portion of the channel, and decay elsewhere. The second point is the remarkably simple relation of that structure to the reference-state flow: large PV variance develops where the horizontal gradient of reference-state PV is large. This relation can be seen by comparing Fig. 7, which shows $|\nabla \overline{q}|$, with Fig. 6c. A similar tendency for large variance where reference-state vorticity or PV gradients are large has been noted previously in other simple models (Gauthier et al. 1993; Tanguay et al. 1995; Fischer et al. 1998).

The perturbation PV variance in the interior develops structure on a similar timescale, as illustrated by Fig. 8a, which shows the fifth model level at $\Delta t = 40$ h. The spatial variations in variance are again clearly related to $|\nabla \overline{q}|$ at the same level (Fig. 8b). In contrast to behavior at the lid, however, PV variance tends to be small (rather than large) where the reference-state PV gradient is large. In addition, PV variance in the interior decays on average (the grayscale in Fig. 8 is reduced by a factor of 10 relative to Figs. 6 or 7), whereas there is significant growth of variance at the lid in regions of large $|\nabla \overline{q}|$.

The relation of the PV variance to the reference-state PV gradients is generic and holds for ensembles initialized at other times as well. The correlation of $\text{Var}(q')$

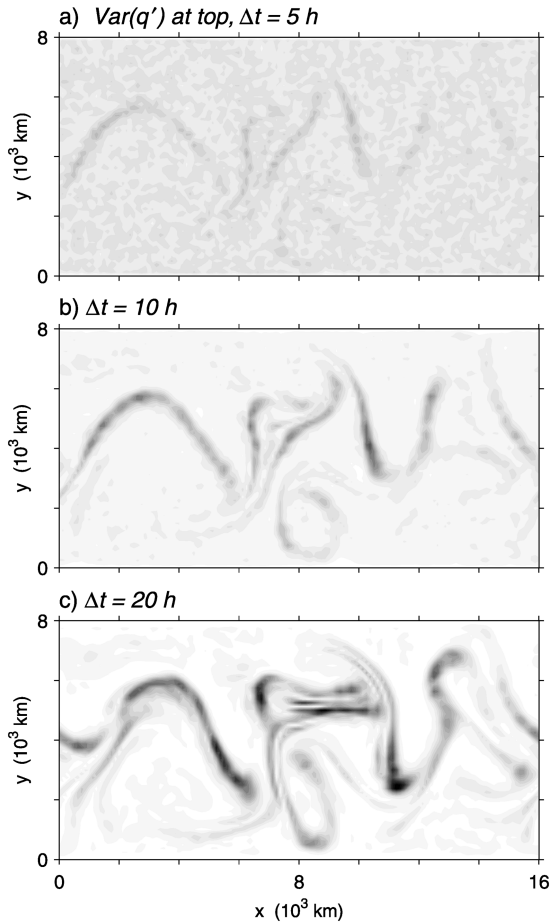a) *Var(q′) at top, Δt = 5 h*

b) *Δt = 10 h*

c) *Δt = 20 h*

FIG. 6. The variance of the generalized q' at the uppermost model level for an ensemble initialized at $t = 120$ days. The variance is shown after time intervals of $\Delta t = 5$, 10, and 20 h [(a), (b) and (c), respectively] and shaded so that white corresponds to zero variance and the darkest gray to the maximum variance in (c).
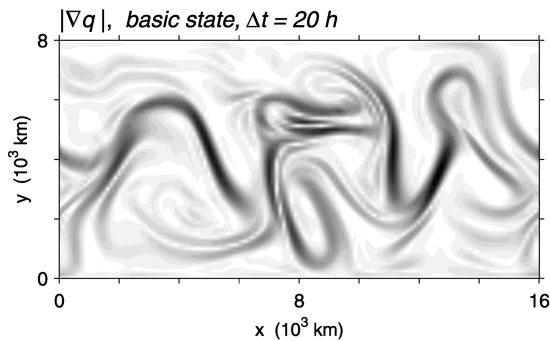
|∇q|, basic state, Δt = 20 h

FIG. 7. The value $|\nabla \overline{q}|$ on the uppermost model level at the same time shown in Fig. 6c ($t = 120$ days $+$ 20 h). The field is shaded so that white corresponds to zero gradient and the darkest gray to the maximum gradients.

a) *Var(q′) at 5th level, Δt = 40 h*
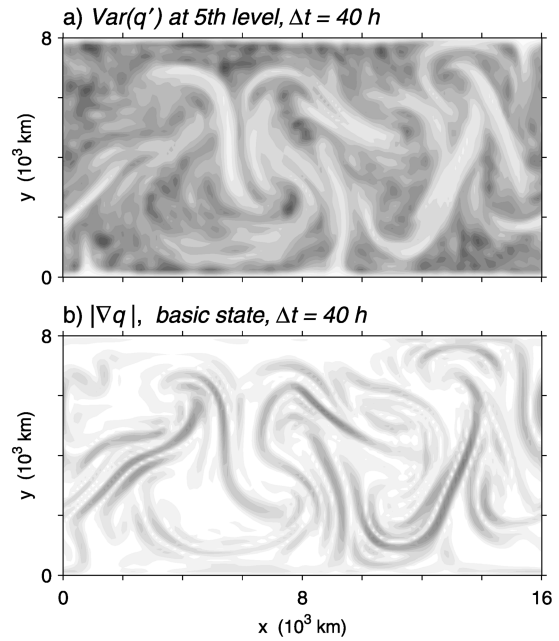
b) *|∇q|, basic state, Δt = 40 h*

FIG. 8. (a) The variance of q' at the fifth model level for an ensemble initialized at $t = 120$ days and a time interval $\Delta t = 40$ h, and (b) $|\nabla \overline{q}|$ on the fifth model level at the time shown in (a) (i.e., $t = 120$ days $+$ 40 h). Shading in (a) and (b) is as in Figs. 6b and 7, respectively, except that the value of the fields corresponding to a given gray shade is reduced by a factor of 10.

and $|\nabla \overline{q}|$ at several levels is shown in Fig. 9 as a function of Δt, averaged over initial times. The PV variance rapidly correlates with $|\nabla \overline{q}|$ at both the top and bottom levels, reaching a maximum near $\Delta t = 1$ day and then asymptoting to a value between 0.5 and 0.6. In the interior, the PV variance develops a negative correlation with the strength of the reference-state gradient over the first two days, which then reverses and ap-
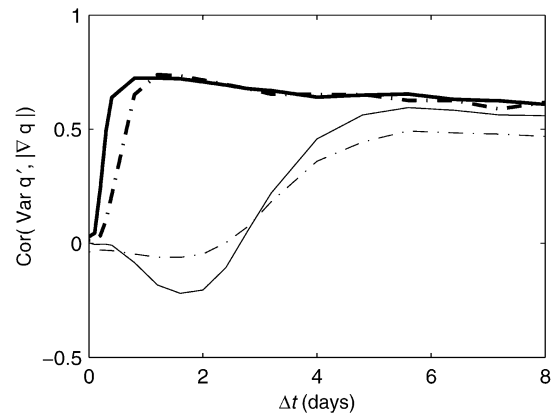
FIG. 9. The correlation of the variance of q' and $|\nabla \overline{q}|$ as a function of time. Correlations are shown for the surface and lid (bold curves; surface, dash–dot lines) and for levels 3 and 5 in the interior (thin curves; level 3, dash–dot). Results are averaged over an ensemble of 10 perturbations and over 10 initial times.
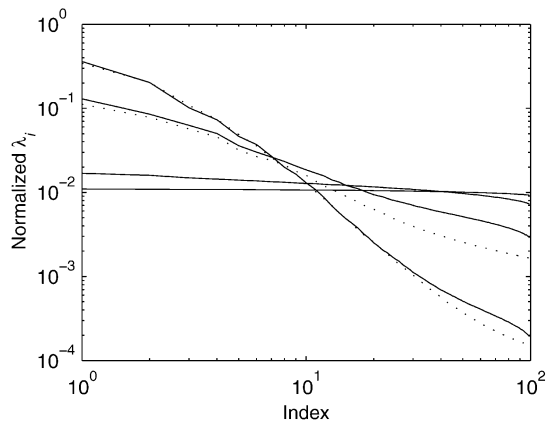
FIG. 10. Eigenvalues λ_i of the sample covariance matrix **P** for 100-member ensembles, normalized by the total variance [i.e., Tr(**P**) = $\Sigma \lambda_i$] and averaged over initial times. Eigenvalues are shown for Δt = 0, 20 h, 2 days, and 4 days; the leading eigenvalue increases monotonically with Δt. Dotted lines show results from 400-member ensemble for Δt = 2 days and 4 days.

proaches a positive value comparable to that at top and bottom.

The perturbation dynamics, including the reasons for the differing behaviors in the interior and at the boundaries and the role of the model's dissipation, are discussed in more detail in section 6.

c. Covariance evolution

Up to this point we have concentrated on the evolution of variances. The spatial (auto) covariances are, of course, also of interest. This section examines the evolution of both global properties of the sample covariance matrices from the ensembles and the local spatial structure of the covariances.

The sample covariance matrix **P** is given by **P** = $(N_e - 1)^{-1}$**XX**^{T}, where N_e is the ensemble size and **X** is the matrix whose N_e columns are the gridpoint PV values of the ensemble members. Since the number of its elements scales as the square of the number of grid points, **P** is too large to manipulate or store even for the QG model, but its $N_e - 1$ nonzero eigenvalues are the singular values of $(N_e - 1)^{-1/2}$**X** and can thus be calculated by singular value decomposition of **X**.

Averaging over initial times, these eigenvalues are shown in Fig. 10 for Δt = 0, 20 h, 2 and 4 days. In the figure, each eigenvalue λ_i is normalized by Tr(**P**) = $\Sigma \lambda_i$, so that they represent the percentage of the total variance accounted for by each eigenvector of **P**.

The eigenvalue spectrum steepens as Δt increases and the ensemble evolves. This steepening again occurs on a timescale of $O(1$ day). The steepening means fewer structures account for a greater percentage of variance within the ensemble; after 2 days, for example, the first 10 eigenvectors explain 43% of the variance. This is

consistent with the rapid appearance of spatial variations in variance as in Fig. 6.

Unlike the other results shown to this point, the sample eigenvalues are subject to noticeable sampling error, particularly soon after the ensemble is initialized. We have repeated the calculations with the ensemble size increased by a factor of 4 (N_e = 400) to quantify the magnitude of the sampling error.

At Δt = 0, the eigenvalues are approximately equal for N_e = 100 (Fig. 10), and quadrupling the ensemble size decreases does not alter this property (not shown). Thus, the initial (normalized) eigenvalues are all approximately N_e^{-1} and changing the ensemble size has a profound effect on any individual eigenvalue. This is a property of sampling in high-dimensional systems: if the ensemble is sufficiently small, and the covariance matrix **C** from which the ensemble is sampled has a spectrum that is not too steep, then the ensemble members are, with high probability, nearly orthogonal. At Δt = 20 h, the situation is simlar, but less severe; increasing N_e to 400 (not shown) steepens the spectrum significantly and decreases the leading eigenvalue by half. Results for Δt = 2 and 4 days are shown with dotted lines in Fig. 10. By these times, the leading eigenvalues show little sensitivity to the ensemble size. Clearly, the sampling errors in the sample eigenvalues decrease dramatically as the ensemble evolves and the spectrum steepens, but unfortunately little theoretical guidance is available to help quantify this dependence.

As shown in the companion paper (Hamill et al. 2002), the spectra of sample analysis- and forecast-error covariance matrices in this system are also steep, rather than flat, again reflecting the influence of the forecast dynamics on such errors. In addition, the steep spectra of the analysis-error covariance illustrates that the initial energy ensemble has little relation to analysis errors, as first suggested in section 2c.

We next turn to the evolution of the spatial structure of the covariances (or correlations) and again focus on q' at the uppermost model level. An example is given in Fig. 11, which shows two-point correlation fields at times Δt = 10, 20, and 40 h following the initialization of the ensemble with 100 members at t = 120 days. Because the correlations are spatially localized, multiple subdomains (the small square boxes) are shown, each of which displays the correlation of q' at the center of that subdomain with q' at surrounding points. Each subdomain covers an array of 21 $\times$ 21 grid points, or an area of 2500^2 km^2.

We have checked the magnitude of sampling errors in Fig. 11 by computing the correlations using an ensemble of 400 members. Although the details of the result change with the larger ensemble, particularly where the correlations are weak, the stronger, short-range correlations are not sensitive to the ensemble size; the rms value of the difference between the 100- and 400-member correlations is 0.091, 0.077, and 0.085 at Δt = 10, 20, and 40 h, respectively. Sampling errors of
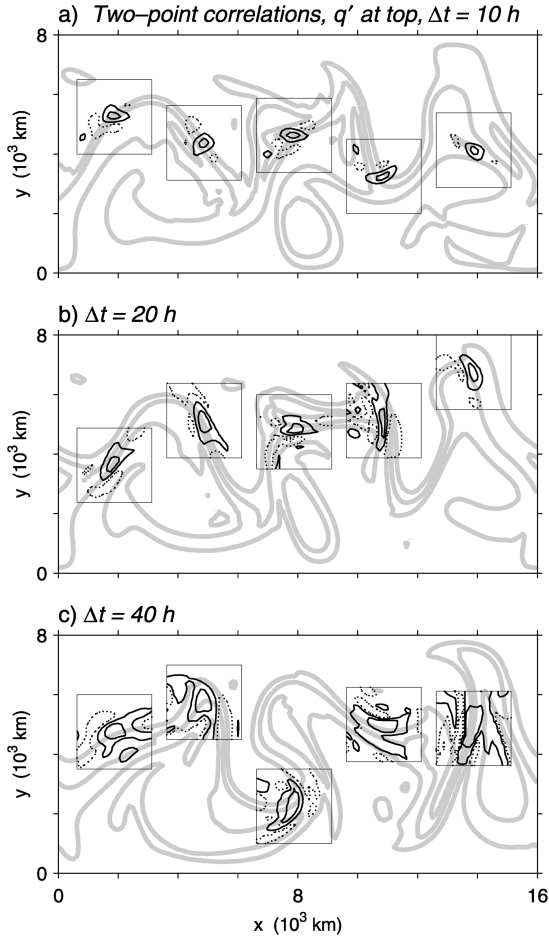
FIG. 11. Two-point correlations for q' at the uppermost model level at three intervals after initialization: $\Delta t = 10$, 20, and 40 h [(a), (b), and (c), respectively]. In each of the smaller square subdomains, contours are shown for the correlation of q' at the center of the box with q' at other locations in the box; these correlations are based on an ensemble of 100 members initialized at $t = 120$ days. Contour values are ± 0.75 and ± 0.25, with dotted lines indicating negative values. The centers of the subdomains are chosen to be equally spaced in x and to coincide with the maximum variance of q' at the zonal location. Contours of $\overline{q}$ at the same times ($t + \Delta t$) are shown in thick gray lines.

this magnitude are consistent with the results of Houtekamer and Mitchell (1998, their Fig. 7) and theory, which predicts sampling errors that are $O(N_e^{-1/2})$.

As was the case for the variances (Fig. 6), the correlations evolve on a timescale of 1–2 days and their evolution appears to bear a strong relation to the reference-state PV. After 10 h (Fig. 11a), the correlations have become anisotropic and typically are strongest along the contours of $\overline{q}$. This tendency becomes pronounced by 20 h (Fig. 11a), with strong correlations extending several hundred kilometers along $\overline{q}$ contours while short-range correlations parallel to $\nabla\overline{q}$ are often negative. The regions of strongest correlations are typically narrow bands that curve to follow the $\overline{q}$ contours;

the correlation structure can be complicated, particularly in regions where $\overline{q}$ has a complicated, layered form. At 40 h (Fig. 11c), the typical correlation length along the reference-state PV contour is comparable to the length scale of the baroclinic waves in the reference state, so that strong correlations often extend from ridge to trough and beyond the bounds of the subdomains shown. The increase of the correlation length is consistent with increase in scale of the perturbations over the first 1–2 days (Fig. 5).

This evolution of the perturbation correlations does not fit the picture of small-scale instabilities developing on a slowly varying large-scale flow, since the development of the perturbations does not produce small-scale structure. Instead, the perturbations quickly assume the reference-state length scales, at least in the direction along $\overline{q}$ contours, and represent shifts or distortions of existing reference-state features. Snyder (1999) and Snyder and Joly (1998) discuss simple mechanisms that can lead to such development.

Although the relation of the correlations to the reference-state PV is difficult to quantify once the spatial structure of the correlations becomes sufficiently complicated (as in Fig. 11c), insight into the initial development of anisotropic correlations can be gained through a simple diagnostic. [Bouttier (1993, p. 413) uses much the same diagnostic and provides further discussion of its formulation.] At each point (x_0, y_0) whose variance is in the top 10% at a given model level, we compute the correlation $C(x, y; x_0, y_0)$ of $q'(x, y)$ with $q'(x_0, y_0)$ and then calculate a local orientation from $C(x, y; x_0, y_0)$ as follows. First, values of the correlation less than 0.25 are set to zero; this avoids complications in interpreting the results when some local correlations are negative and makes the diagnostic more robust. Then, the moments

$$a(x_0, y_0) = \int (x - x_0)^2 C(x, y; x_0, y_0)\, dA,$$

$$b(x_0, y_0) = \int (y - y_0)^2 C(x, y; x_0, y_0)\, dA,$$

$$c(x_0, y_0) = \int (x - x_0)(y - y_0) C(x, y; x_0, y_0)\, dA,$$

are calculated as summations over the 11×11 array of grid points centered at (x_0, y_0). Finally, the local orientation is defined by the vector $[2c, -(a - b) + ((a - b)^2 + 4c^2)^{1/2}]$. If $C(x, y; x_0, y_0)$ is constant along concentric ellipses of fixed orientation in the (x, y) plane, then this vector lies parallel to the ellipses' major axes.

Figure 12 shows the probability distribution, averaged over initial times, for the angle between $\nabla\overline{q}$ and the local orientation of the correlation at the top model level. The evolution of the probability density function (pdf) confirms that the behavior shown in Fig. 11 is generic. Although they are initially nearly isotropic, the local
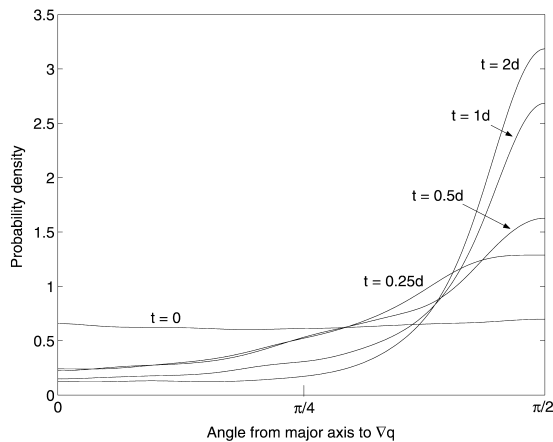
FIG. 12. Probability density function of the angle between $\nabla \overline{q}$ and the local orientation of the spatial autocorrelation of q' at the uppermost model level. Each curve is labeled with Δt.

correlations develop significant anisotropy within the first day and, by 2 days, the orientations of the correlation is overwhelmingly along contours of $\overline{q}$ (and normal to $\nabla \overline{q}$, so that the angle displayed in Fig. 12 is approximately $\pi/2$). The dynamics that lead to the development of anisotropy are discussed in section 6.

Finally, we note that these results provide some justification for existing, empirical models of the flow dependence of forecast-error covariances. Riishøjgaard (1998) proposes a correlation model in which error correlations are enhanced along isolines of the analyzed variable; such a model will provide correlations that are qualitatively similar to Fig. 11, where the correlation of PV perturbations tend to follow contours of the reference-state PV. To the extent that the relation (2) results in streamlines that follow PV contours, Fig. 11 is also qualitatively consistent with models that enhance correlations in the direction of the local flow, such as Benjamin and Seaman (1985).

d. Other initial ensembles

It is natural to ask how the initial statistics of the ensemble influence the results presented earlier. In addition to the energy ensemble, we have also computed the diagnostics of sections 4b and 4c (except for that shown in Fig. 12) for four other initial ensembles: the potential-enstrophy and streamfunction ensembles, and the two truncated energy ensembles ($k_c = 16$ and 32) discussed in relation to Fig. 3.

These initial ensembles span a range of possibilities. In the potential-enstrophy ensemble, the largest vertical and horizontal scales have greater (expected) amplitude, and the smaller scales smaller amplitude, relative to the energy ensemble. The streamfunction ensemble has the opposite relation to the energy ensemble, with a flatter power spectrum and more amplitude in the smallest scales. The truncated energy ensembles resemble the

enstrophy ensemble in that their velocity fields are dominated by large scales, but differ in that small vertical scales are retained.

Despite these differences, the evolution of all five ensembles agrees in important respects. First, each ensemble develops qualitatively similar characteristics, such as potential enstrophy that is strongly peaked at the top and bottom boundaries (as in Fig. 3), strong correlation between Var(q') and $|\nabla \overline{q}|$ (as in Fig. 9), and a steep eigenvalue spectrum for the sample covariance matrix (as in Fig. 10). Second, these characteristics develop on the same timescale of 1–3 days found for the energy ensemble.

Some details of the initial evolution, of course, differ among the ensembles. Because it is controlled by the dissipation small scales (see section 4a and Fig. 3), the initial decay of the perturbations depends sensitively on the relative amplitudes of small and large scales in the ensemble. Thus, the streamfunction ensemble, with more amplitude in small horizontal scales, exhibits a greater initial decay of energy than that shown in Fig. 3, while the potential-enstrophy ensemble decays less rapidly. The development of correlation between Var(q') and $|\nabla \overline{q}|$ is also slightly slower and the steepening of eigenvalue spectrum is weaker for the streamfunction ensemble than the energy ensemble, and the potential-enstrophy or truncated energy ensembles again have the opposite behavior, with more rapid development of the correlation between Var(q') and $|\nabla \overline{q}|$ and a steeper eigenvalue spectrum. We emphasize, however, that these are differences in detail and, in all cases, the gross characteristics of the ensemble are similar after 3–4 days regardless of their initial statistics.

The fact that the qualitative characteristics of the ensemble become insensitive to its initial statistics is consistent with the behavior of the leading singular vectors over similar time intervals in other studies. For example, Palmer et al. (1998) show that, while the initial structure of the leading singular vectors depends strongly on the choice of norm, their evolved structure after 2 days is relatively insensitive to that choice. (Recall from section 2c that specifying the initial statistics of the ensemble corresponds to choosing the initial-time norm in a singular-vector calculation.)

5. Convergence to the leading Lyapunov vectors

As noted in the introduction, there is a considerable body of dynamical-systems theory applicable to our ensemble experiments in the limit $\Delta t \to \infty$. In particular, almost any ensemble of N perturbations converges in that limit to the subspace spanned by the N leading Lyapunov vectors, which vary in time but depend only on the reference solution (and the inner product chosen to calculate projections). The fate of the ensemble is thus, at least asymptotically, largely determined by its dynamical evolution and independent of its initial statistics. Legras and Vautard (1995) provide further back-
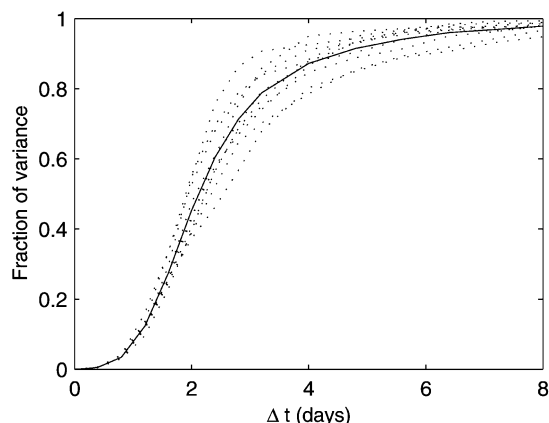
FIG. 13. Fraction of the sample variance explained by the first 20 Lyapunov vectors as a function of Δt. Results are shown for 10 initial times (dotted lines) and for the average over initial times (solid). The sample variance is calculated in terms of total energy.

ground and references on Lyapunov stability of dynamical systems.

It is not obvious that the asymptotic properties defined by the leading Lyapunov vectors should be relevant to the ensembles considered here, where Δt is not large. Note, however, that the many properties of the perturbations after a day or two do resemble the gross structure of the leading Lyapunov vectors for this system as documented by SH. These properties include horizontal scales comparable to that of reference state, perturbation PV concentrated at the upper and lower boundaries, significant spatial correlation between squared perturbation PV and $|\nabla \overline{q}|$, and much longer (auto) correlation lengths along $\overline{q}$ contours than normal to them. This similarity suggests that there has been substantial convergence toward the leading Lyapunov vectors even after 1–2 days.

A simple measure of the ensembles' convergence to a given subspace is the fraction of variance explained by that subspace. This is calculated by projecting each perturbation onto the subspace and comparing the variance of the projection with that of the original ensemble. Here, the subspace will be defined by the first 20 Lyapunov vectors and projections are based on the total-energy inner product. The fraction of variance is shown as a function of Δt in Fig. 13, both for 10 specific initial times (dotted lines) and averaged over those initial times (solid).

The variance explained by the first 20 Lyapunov vectors initially increases rapidly, reaching about 0.8 by after 2.5 days, and then asymptotes more slowly to 1 at longer times. Clearly, the timescale of 1–2 days for the initial, transient evolution of the ensemble is comparable to that for the convergence of the ensemble perturbations to the subspace spanned by the leading Lyapunov vectors (or more generally, to the unstable manifold defined by the Lyapunov vectors with positive

exponents), and the Lyapunov vectors contain considerable information about the ensemble even on timescales relevant to numerical weather prediction.

This timescale for the emergence of significant projection on the leading Lyapunov vectors is consistent with results from other quasigeostrophic studies. Swanson et al. (1998) find that, at the end of a 5-day interval of four-dimensional variational assimilation, roughly one-half of the analysis-error variance is explained by the first 100 Lyapunov vectors. In addition, Reynolds and Errico (1999) have shown that the leading Lyapunov vector has a strong projection on the subspace of the first 30 evolved singular vectors even for optimization times of 5 days.

An additional point is that the strong convergence shown in Fig. 13 requires projecting on not just the single leading Lyapunov vector, but on a subspace spanned by many Lyapunov vectors. Even at $\Delta t = 8$ days, the perturbations have not converged to the single, most rapidly growing Lyapunov vector. Instead, the projection is spread over the entire subspace; at $\Delta t = 8$ days, the first, third, and fifth LVs on average account for 25%, 14%, and 10% of the variance.

6. Perturbation dynamics

To this point, we have seen that the growth of perturbations becomes on average, exponential following a transient period of 1–3 days, and that this same transient period is associated with changes from the initial spatial structure (implied by the chosen covariance matrix **C**) to a dynamically determined structure whose characteristics are largely independent of the initial conditions. In particular, perturbations evolve to have PV concentrated at the top and bottom boundaries (with little PV in the interior of the flow); on those boundaries the perturbation PV becomes strongly correlated with the magnitude of the reference-state PV gradients, and anisotropic covariances develop, with the strongest spatial correlations extending along contours of the reference-state PV. This section examines the dynamics that give rise to such behavior.

a. Role of $\nabla \overline{q}$

We begin by examining the reasons for the strong relation of the perturbations to the reference-state PV gradient and, in particular, why that relation differs from the upper and lower boundaries to the interior.

The perturbation dynamics are governed by (8). Aside from relaxation and dissipation, perturbation PV evolves through two processes: the advection of q' by the reference-state flow and the advection of $\nabla \overline{q}$ by the perturbations. An evolution equation for $\mathrm{Var}(q')$ can be derived by multiplying (8) by q' and taking expected values, which yields

$$(\partial_t + \overline{\mathbf{v}} \cdot \nabla) \, \mathrm{Var}(q') + 2\langle \mathbf{v}'q' \rangle \cdot \nabla \overline{q}$$

$$= -\mathrm{Var}(q')/\tau + \langle q'Dq' \rangle, \qquad (9)$$

where $\langle \cdot \rangle$ denotes the expected value and the perturbations are assumed to have zero mean.

The reference-state advections simply rearrange the variance field, while the relaxation and (typically) the dissipation are sinks for $\mathrm{Var}(q')$. The advection of $|\nabla \overline{q}|$ by the perturbations in (8) gives rise to a source for $\mathrm{Var}(q')$ where $\nabla \overline{q} \neq 0$ and there is a downgradient PV flux ($\langle \mathbf{v}'q' \rangle$ and $\nabla \overline{q}$ oppositely directed). This source is clearly crucial to the evolution of $\mathrm{Var}(q')$ at the top and bottom boundaries, since $\mathrm{Var}(q')$ grows and is concentrated where $\nabla \overline{q}$ is large (Fig. 6). Both Thompson (1986) and Evensen (1992) also identify the interaction of the error velocities with the reference-state PV gradients as the key process in the evolution of initially isotropic errors.

The different evolution of $\mathrm{Var}(q')$ at the boundaries as compared to the interior arises from differences in the source term between different levels. At the upper and lower boundaries, $|\nabla \overline{q}|$ is large compared to its value throughout the interior of the flow, in terms of both local maxima and net cross-channel change. The initial amplitude of either q' or $\mathbf{v}'$, in contrast, varies little with height. Thus, other things being equal (such as the anisotropy of the covariances, which leads to nonzero $\langle \mathbf{v}'q' \rangle$), the source term for $\mathrm{Var}(q')$ will be largest at the boundaries. Examination of each term in (9) in the early stages of the numerical solutions (not shown) confirms that, at top and bottom, the source term controls the evolution of $\mathrm{Var}(q')$ wherever $|\nabla \overline{q}|$ is large, while the dissipation dominates elsewhere.

In the interior, the reference-state PV gradients are weak enough that the source term is of secondary importance and q' behaves as a passive scalar that is advected and dissipated. (Note from Figs. 7 and 8b that the largest interior gradients are more than a factor of 20 smaller than at the lid, while Fig. 4 indicates that perturbation velocities decrease by little more than a factor of 2 from the lid to the interior.) Ignoring dissipation for the moment, such a scalar field will develop smaller and smaller scales with time as material lines are deformed and stretched by the advecting flow, and this development of small scales will occur preferentially where the flow has largest strain. There is then enhanced dissipation in these regions, leading to the development of spatial structure in $\mathrm{Var}(q')$ [Fig. 8; see Fig. 5 of Evensen (1992) for a similar result]. Because the same straining flow also advects the reference-state PV and typically increases its gradient, regions of large strain also correspond, to a first approximation, to regions of large $|\nabla \overline{q}|$. Thus, the interior perturbations evolve over the first 1–2 days so that $\mathrm{Var}(q')$ and $|\nabla \overline{q}|$ are anticorrelated (Figs. 8,9).

After 4–6 days, however, this relation reverses and $\mathrm{Var}(q')$ in the interior becomes correlated with $|\nabla \overline{q}|$ as at the boundaries (Fig. 9). This is because the variance decays in the interior while growing at the boundaries (Fig. 4); $\mathbf{v}'$ in the interior is then determined by the perturbation PV at the boundaries rather than that in the interior, and does not decay. In this regime, the source term becomes important in the interior, since the variance is now very small, and $\mathrm{Var}(q')$ begins to correlate positively with $|\nabla \overline{q}|$. The small amount of interior q' and its structure are in any case not central to the behavior of the perturbations at this stage, but instead are driven by the evolution of q' at the boundaries.

b. Role of dissipation

Given that the initial decay of the perturbation energy occurs on a timescale similar to that for the covariance evolution, and that initial decay is controlled by the dissipation, it is natural to ask the extent to which the dissipation also contributes to aspects of the covariance evolution, such as the emergence of spatial variations in $\mathrm{Var}(q')$. We will focus on the role of the numerical smoothing, as this is both the dominant and most poorly justified contributor to dissipating the PV.

First, it is clear that the dissipation does not directly control the covariance evolution, even for small Δt. If the ensembles are evolved subject only to the dissipation [ignoring the advective terms in (8)], the perturbations develop none of the characteristic structure seen previously (e.g., in Figs. 4, 5, 6, 9, and 11). Moreover, if small scales are truncated from the initial ensemble ($k_c = 16$, as in Fig. 3) so that the numerical smoothing is initially a small effect, spatial variations appear even more rapidly in the PV variance (not shown).

A more direct test of the influence of the numerical smoothing is to repeat the experiments described in section 4 with the model resolution doubled and ν reduced by a factor of 8. To allow a direct comparison with results in section 4, the ensemble perturbations for these doubled-resolution experiments are drawn from the same population as in the original experiments; that is, the perturbations have power only at scales resolved in the original experiments.

The principal difference in results is that the initial decay of the perturbation energy is greatly reduced at doubled resolution (not shown). While the energy again reaches a minimum after about 20 h, it is reduced at doubled resolution by only 20% relative to its initial value (as opposed to a reduction of almost a factor of 3 in Fig. 3). This weaker initial decay again shows, as in Fig. 3, that the dissipation controls the decay—the perturbations have the same scales as in the original experiment but the numerical smoothing is reduced by a factor of 8 at doubled resolution, so the initial decay of the perturbation is slower.

In other respects, the perturbation evolution is qualitatively unchanged: the potential enstrophy still grows rapidly at the boundaries while decaying in the interior (as in Fig. 4), perturbations still develop an energy spectrum
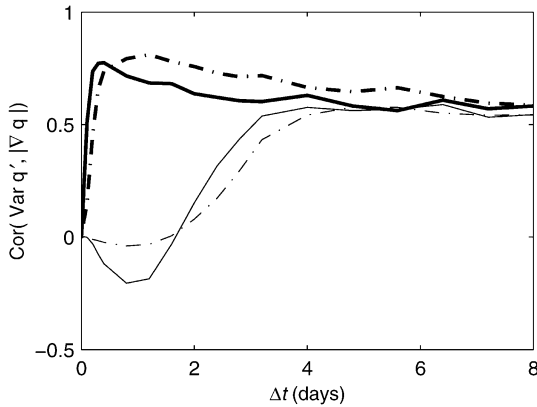
FIG. 14. As in Fig. 9 but for the experiments at doubled resolution.

that peaks around wavenumber 5 (as in Fig. 5), and Var(q') again has a strong correlation with $|\nabla\overline{q}|$. This last point is illustrated by Fig. 14, which shows the correlation of Var(q') and $|\nabla\overline{q}|$ as a function of Δt for the doubled-resolution experiments and should be compared with Fig. 9. Thus, consistent with our arguments in section 6a earlier, it is the advective dynamics, and not the dissipation, that controls the covariance evolution.

7. Summary and discussion

We have adopted an experimental approach to understanding the dynamics of forecast-error covariances. Because of the difficulty of this problem, our exploration has been limited to linear dynamics.

The experiments begin with a quasigeostrophic simulation of statistically steady, turbulent flow driven by relaxation to an unstable baroclinic jet. This reference flow consists of a strong jet disturbed by baroclinic waves and qualitatively resembles midlatitude tropospheric flow. Ensembles of perturbations are then drawn from a Gaussian distribution with (nearly) homogeneous and isotropic covariance matrix, and evolved under dynamics linearized about the reference solution. The sample covariances based on these ensembles provide estimates of the true covariance evolution arising from the specified initial covariances. Because the results are based on a dry, quasigeostrophic model, we expect them to be applicable qualitatively, but probably not in detail, to flows at synoptic and larger scales in primitive equation models.

The linear dynamics impose significant structure on the perturbations and their covariances on a timescale of roughly a day. This timescale, which is comparable to the advective timescale for the reference flow, defines an initial, transient period during which the perturbations and their covariances tend to a characteristic form that is insensitive to the specified initial covariances.

In terms of perturbations' gross structure, the potential enstrophy becomes concentrated at the surface and the tropopause (or at the lid of the present model) where gradients of $\overline{q}$ are large. Perturbation winds and poten-

tial temperature are maximized at the surface and lid and decay slowly into the interior. This structure follows from inversion of the PV through (2). In addition, the horizontal scale of the perturbations becomes comparable to that of reference state over the initial 1–2 days: power at small scales decays rapidly, while larger scales (comparable to reference state) begin to grow.

The detailed spatial structure of the perturbations and their covariances are also strongly shaped by the dynamics during this initial period. At the surface and lid, where $\nabla\overline{q}$ is much larger than in the interior, Var(q') rapidly (within 10 h) becomes strongly correlated in space with $|\nabla\overline{q}|$. Spatial correlations become anistropic on the same timescale, with the strongest correlations extending along contours of $\overline{q}$. In the interior, however, the initial behavior of the PV variance is just the opposite, with minima tending to coincide with regions of large $\nabla\overline{q}$; beyond roughly 2 days of evolution this behavior reverses and Var(q') becomes correlated with $\nabla\overline{q}$.

The evolution equations for perturbation PV (8) and it variance (9) provide an explanation for the behavior of q'. Since the advection by the reference-state flow conserves Var(q'), the growth of PV variance and the development of its characteristic structure must arise from perturbation advection of $\nabla\overline{q}$; diagnostic calculations in the simulations confirm this. Thus, the behavior of the perturbations and their statistics appears to be fundamentally controlled by the reference-state PV gradients, which are small in the interior compared to either top or bottom boundaries. (The PV of the midlatitude troposphere has qualitatively similar structure.) The large gradients at the surface and lid, coupled with the fact that perturbations anywhere in the domain produce significant flow at the boundaries, imply that, for short times, there is a substantial source of PV variance on either boundary, while that in interior is relatively weak. As a consequence, Var(q') at the boundaries rapidly becomes correlated with $|\nabla\overline{q}|$ and q' takes the form of elongated bands along the narrow fronts where $\nabla\overline{q}$ is large. The perturbation PV in the interior, by contrast, is simply advected by the reference-state flow, with the result that it is deformed to smaller scales and dissipated in regions of strong reference-state strain. Since the strain tends to be strong where $\nabla\overline{q}$ is large, Var(q') in the interior initially tends to be small (rather than large, as on boundaries) where $\nabla\overline{q}$ is large. The characteristic correlation structure, which is elongated along reference-state PV contours, also arises from the pertubation advection of $\nabla\overline{q}$: Because perturbations have scales comparable to the reference state, perturbation advections tend to be coherent along the reference-state PV contours and to produce PV perturbations that extend along those contours.

Snyder and Joly (1998) and Snyder (1999) provide other, more idealized examples of this mechanism for error growth, in which perturbations are coherent on the spatial scale of the reference state and perturbation advections lead to displacements or distortions of existing

features in the reference state. An alternative explanation is that the error growth arises from a local shear instability supported by strong gradients of the reference-state PV (e.g., Lilly 1972; Gauthier et al. 1993). Our results, particularly the fact that the growing perturbations rapidly adopt a horizontal scale comparable to that of the reference state, do not support the shear-instability explanation.

We have also shown that the perturbations converge to the subspace of the leading Lyapunov vectors on a timescale of $O(1$ day), which is roughly the same as that typifying the covariance evolution. Thus, the characteristic form of the forecast-error covariances is closely related to the structure of perturbations on the unstable manifold and knowledge of the leading Lyapunov vectors could potentially be used to infer qualitative features of the covariances.

The general features of the forecast-error covariances (such as the typical vertical structure and horizontal scale) are easily captured by ensembles of 10 members, as is the strong relation between the PV variance and $\nabla \overline{q}$. With an ensemble of $N_e = 100$ members, the spatial structure of variances and correlations can be reliably estimated; the errors in the estimated correlations appear to be $O(N_e^{-1/2})$, consistent with the arguments and results of Houtekamer and Mitchell (1998). Since the state vector for this system has dimension of order 10^5, it is clear that the use of ensembles much smaller than the state dimension is not a fundamental obstacle to estimating the error covariances.

The experiments presented here show that, in quasigeostrophic flow, error covariances evolve rapidly to become strongly anisotropic and that such anisotropy is intimately related to the state of the reference flow. A companion paper (Hamill et al. 2002) demonstrates that such dynamically determined structure survives the assimilation of new observations (i.e., the analysis process) to a substantial extent. Thus, it is likely that present assimilation schemes could be significantly improved through the use of flow-dependent, anisotropic estimates of forecast-error (or background) covariances. One possible approach is to develop an empirical covariance model [similar to Benjamin and Seaman (1985) or Riishøgaard (1998)], based on the tendencies for error variance to be largest where the reference-state PV gradient is large and for error correlations (both positive and negative) to be enhanced along contours of the reference-state PV. Another approach is to tune an anisotropic covariance model based on information from an ensemble of forecasts (J. Purser 2000, personal communication). However, given that even relatively small ensembles can provide useful local estimates of forecast-error covariances, the most promising approach

may well be to incorporate the sample covariances from the ensemble directly into the assimilation scheme, and in turn allow the assimilation process to update the forecast ensemble given new observations (Evensen 1994; Houtekamer and Mitchell 1998; Hamill and Snyder 2000).

APPENDIX

Inner Products and Sampling Procedures

The inner products used here are based on the squared streamfunction, the total energy, and the potential enstrophy. The inner product of two states ϕ_1 and ϕ_2 are calculated as discrete approximations to the integrals $\int \phi_1 \phi_2 \, dV$ for squared streamfunction, $\int \nabla \phi_1 \cdot \nabla \phi_2 \, dV$ for total energy, and $\int \tilde{q}_1 \tilde{q}_2 \, dV$ for potential enstrophy, where $\tilde{q} = \nabla^2 \phi + [\delta(z) - \delta(z-1)]\phi_z$ is the generalized PV.

In all cases, we use second-order approximations to the integrals (i.e., Simpson's rule). In particular, values at $y = 0$, y_L and $z = 0$, 1 are weighted by one-half in the discrete summation. Streamfunction and PV are taken directly from the model grid. For energy, spatial derivatives of ϕ are calculated on a staggered grid (x derivatives, for example are staggered in x) as differences between adjacent grid points of ϕ.

Although the inner products are readily calculated using the gridpoint values of the fields, sampling from the distributions discussed in section 2c is most easily accomplished using a Fourier representation. This is because the matrix **S** defining the inner product on the grid points may be singular (e.g., a constant field has zero energy) and its domain need not be restricted to perturbations satisfying the boundary conditions (6). The desired Fourier basis should satisfy the boundary conditions and should be orthogonal under the chosen inner products. This orthogonality simplifies the sampling procedure, as samples from $N(\mathbf{0}, \mathbf{C})$ may then be constructed by multiplying each basis function by an independent random number drawn from a normal distribution with appropriate variance, and summing over the basis.

Such a basis can be written in the form $b(\hat{k}, k)c(\hat{m}, m) d(\hat{n}, n)$, where k, m, and n are x, y, and z wavenumbers, respectively, and $\hat{k}$, $\hat{m}$, and $\hat{n}$ are gridpoint indices. Let K, M, N be the corresponding numbers of grid points. The required functions are then

$$b(\hat{k}, k) = K^{-1/2} \exp(i\hat{k}k2\pi/K),$$

for $\hat{k} = 0, \ldots, K - 1$ and $K = 0, \ldots, K - 1$, and

$$d(\hat{n}, n) = \begin{cases} N^{-1/2} & \text{if } n = 0; \\ (N/2)^{-1/2} \cos[n(\hat{n} - 1/2)\pi/N] & \text{if } n = 1, \ldots, N - 1; \end{cases}$$

for $\hat{n} = 1, \ldots, N$. When $k = 0$,

$$c(\hat{m}, m)$$

$$= \begin{cases} (M/2)^{-1/2} \cos(m\hat{m}\pi/M) & \text{if } m = 1, \ldots, M-1; \\ M^{-1/2} \cos(\hat{m}\pi) & \text{if } m = M; \end{cases}$$

for $\hat{m} = 0, \ldots, M$; when $k > 0$,

$$c(\hat{m}, m) = (M/2)^{-1/2} \sin(m\hat{m}\pi/M)$$

for $m = 1, \ldots, M-1$ and $\hat{m} = 0, \ldots, M$.

To sample from the distribution corresponding to the squared streamfunction inner product, we set

$$\phi' = \sum_{k,m,n} a_{kmn} b(\hat{k}, k) c(\hat{m}, m) d(\hat{n}, n),$$

and sample each amplitude a_{kmn} from $N(0, 1)$. For the energy inner product, a_{kmn} is sampled from $N(0, \sigma^2)$, where

$$\sigma^2 = 2(3 - \cos k\pi/K - \cos m\pi/M - \cos n\pi/N).$$

The sampling for potential enstrophy proceeds as for the squared streamfunction, but the generalized PV is expanded in the basis functions. In all cases, the variance of a_{kmn} is given by the norm of the basis function using the chosen inner product.

REFERENCES

Arakawa, A., 1966: Computational design for long-term numerical integration of the equations of fluid motion: Two-dimensional incompressible flow. Part I. *J. Comput. Phys.,* **1,** 119–143.

Benjamin, S. G., and N. L. Seaman, 1985: A simple scheme for objective analysis in curved flow. *Mon. Wea. Rev.,* **113,** 1184–1198.

Boer, G. J., and T. G. Shepherd, 1983: Large-scale two-dimensional turbulence in the atmosphere. *J. Atmos. Sci.,* **40,** 164–184.

Bouttier, F., 1993: The dynamics of error covariances in a barotropic model. *Tellus,* **45A,** 408–423.

Bretherton, F. P., 1966: Critical layer instability in baroclinic flows. *Quart. J. Roy. Meteor. Soc.,* **92,** 325–334.

Cohn, S. E., 1993: Dynamics of short-term univariate forecast error covariances. *Mon. Wea. Rev.,* **121,** 3123–3149.

Davis, C. A., 1992: A potential vorticity diagnosis of the importance of initial structure and condensational heating in observed extratropical cyclogenesis. *Mon. Wea. Rev.,* **120,** 2409–2428.

Errico, R. M., T. Vukicevic, and K. Raeder, 1993: Examination of the accuracy of a tangent linear model. *Tellus,* **45A,** 462–477.

Evensen, G., 1992: Using the extended Kalman filter with a multilayer quasi-geostrophic ocean model. *J. Geophys. Res.,* **97** (C11), 17 905–17 924.

——, 1994: Sequential data assimilation with a nonlinear quasi-geostrophic model using Monte Carlo methods to forecast error statistics. *J. Geophys. Res.,* **99** (C5), 10 143–10 162.

Fischer, C., A. Joly, and F. Lalaurette, 1998: Error growth and Kalman filtering within an idealized baroclinic flow. *Tellus,* **50A,** 596–615.

Gauthier, P., P. Courtier, and P. Moll, 1993: Assimilation of simulated wind lidar data with a Kalman filter. *Mon. Wea. Rev.,* **121,** 1803–1820.

Gilmour, I., L. A. Smith, and R. Buizza, 2001: On the duration of the linear regime: Is 24 hours a long time in synoptic weather forecasting? *J. Atmos. Sci.,* **58,** 3525–3539.

Hamill, T. M., and C. Snyder, 2000: A hybrid ensemble Kalman filter/

3D-variational analysis scheme. *Mon. Wea. Rev.,* **128,** 2905–2919.

——, ——, and R. E. Morss, 2002: Analysis-error statistics of a quasigeostrophic model using three-dimensional variational assimilation. *Mon. Wea. Rev.,* **130,** 2777–2790.

Hollingsworth, A., and P. Lönnberg, 1986: The statistical structure of short-range forecast errors as determined from radiosonde data. Part I: The wind field. *Tellus,* **38A,** 111–136.

Hoskins, B. J., and N. V. West, 1979: Baroclinic waves and frontogenesis. Part II: Uniform potential vorticity jet flows—Cold and warm fronts. *J. Atmos. Sci.,* **36,** 1663–1680.

——, M. E. McIntyre, and A. W. Robertson, 1985: On the use and significance of insentropic potential vorticity maps. *Quart. J. Roy. Meteor. Soc.,* **111,** 877–946.

Houtekamer, P. L., and H. L. Mitchell, 1998: Data assimilation using an ensemble Kalman filter technique. *Mon. Wea. Rev.,* **126,** 796–811.

Lee, S., and I. M. Held, 1993: Baroclinic wave packets in models and observations. *J. Atmos. Sci.,* **50,** 1413–1428.

Legras, B., and R. Vautard, 1995: A guide to Lyapunov vectors. *Proc. Seminar on Predictability,* Reading, United Kingdom, ECMWF, Vol. 1, 143–156.

Lilly, D. K., 1972: Numerical simulation studies of two-dimensional turbulence. II. Stability and predictability studies. *Geophys. Fluid Dyn.,* **4,** 1–28.

Molteni, F., R. Buizza, T. N. Palmer, and T. Petroliagis, 1996: The ECMWF Ensemble Prediction System: Methodology and validation. *Quart. J. Roy. Meteor. Soc.,* **122,** 73–119.

Palmer, T. N., R. Gelaro, J. Barkmeijer, and R. Buizza, 1998: Singular vectors, metrics, and adaptive observations. *J. Atmos. Sci.,* **55,** 633–653.

Pedlosky, J., 1987: *Geophysical Fluid Dynamics.* Springer-Verlag, 710 pp.

Peixoto, J. P., and A. H. Oort, 1992: *Physics of Climate.* American Institute of Physics, 520 pp.

Reynolds, C. A., and R. M. Errico, 1999: Convergence of singular vectors toward Lyapunov vectors. *Mon. Wea. Rev.,* **127,** 2309–2323.

Riishøjgaard, L. P., 1998: A direct way of specifying flow-dependent background error correlations for meteorological analysis systems. *Tellus,* **50A,** 42–57.

Rotunno, R., and J.-W. Bao, 1996: A case study of cyclogenesis using a model hierarchy. *Mon. Wea. Rev.,* **124,** 1051–1066.

Snyder, C., 1999: Error growth in flows with finite-amplitude waves or other coherent structures. *J. Atmos. Sci.,* **56,** 500–506.

——, and A. Joly, 1998: Development of perturbations within a growing baroclinic wave. *Quart. J. Roy. Meteor. Soc.,* **124,** 1961–1983.

——, and T. M. Hamill, 2003: Leading Lyapunov vectors of a turbulent baroclinic jet in a quasigeostrophic model. *J. Atmos. Sci.,* in press.

Swanson, K. L., R. Vautard, and C. Pires, 1998: Four-dimensional variational assimilation and predictability in a quasi-geostrophic model. *Tellus,* **50A,** 369–390.

Tanguay, M., P. Bartello, and P. Gauthier, 1995: Four-dimensional data assimilation with a wide range of scales. *Tellus,* **47A,** 974–997.

Thompson, P. D., 1986: A simple approximate method of stochastic-dynamic prediction for small intial errors and short range. *Mon. Wea. Rev.,* **114,** 1709–1715.

Todling, R., and M. Ghil, 1994: Tracking atmospheric instabilities with the Kalman filter. Part I: Methodology and one-layer results. *Mon. Wea. Rev.,* **122,** 183–204.

Toth, Z., and E. Kalnay, 1997: Ensemble forecasting at NCEP and the breeding method. *Mon. Wea. Rev.,* **125,** 3297–3319.

Wirth, A., and M. Ghil, 2000: Error evolution in the dynamics of an ocean general circulation model. *Dyn. Atmos. Oceans,* **32,** 419–431.